

# Growth and low-energy electron microscopy characterization of monolayer hexagonal boron nitride on epitaxial cobalt

Carlo M. Orofeo, Satoru Suzuki, Hiroyuki Kageshima, and Hiroki Hibino (✉)

NTT Basic Research Laboratories, NTT Corporation, Atsugi, Kanagawa 243-0198 Japan

**Received:** 5 February 2013

**Revised:** 18 March 2013

**Accepted:** 19 March 2013

© Tsinghua University Press  
and Springer-Verlag Berlin  
Heidelberg 2013

## KEYWORDS

chemical vapor deposition,  
cobalt,  
domain boundaries,  
hexagonal boron nitride,  
low-energy electron  
microscopy (LEEM)

## ABSTRACT

Low-energy electron microscopy (LEEM) has been used to study the structure, initial growth orientation, growth progression, and the number of layers of atomically thin hexagonal boron nitride (h-BN) films. The h-BN films are grown on **heteroepitaxial Co using chemical vapor deposition (CVD) at low pressure.** Our findings from LEEM studies include the growth of monolayer film having two, oppositely oriented, triangular BN domains commensurate with the Co lattice. The growth of h-BN appears to be self-limiting at a monolayer, with thicker domains only appearing in patches, presumably initiated between domain boundaries. Reflectivity measurements of the thicker h-BN films show oscillations resulting from the resonant electron transmission through quantized electronic states of the h-BN films, with the number of minima scaling up with the number of h-BN layers. First principles density functional theory (DFT) calculations show that the positions of oscillations are related to the electronic band structure of h-BN.

## 1 Introduction

The isolation of graphene, an atomically thin two-dimensional (2D) crystal, in 2004 has sparked much interest in the exploration of other 2D materials [1, 2]. Among the 2D materials, hexagonal boron nitride (h-BN) has also attracted much attention due to its various applications, ranging from dielectric layers and transparent membranes to UV emitters [3–6]. h-BN has a hexagonal structure very similar to graphene having a lattice mismatch of less than 2% [7]. However,

instead of an all-carbon hexagonal lattice, h-BN is composed of alternating  $sp^2$ -bonded boron and nitrogen atoms. The small lattice mismatch, along with its atomically flat surface and inertness to charge impurities, makes h-BN a suitable substrate for graphene electronics. For example, h-BN acting as an intermediate material between graphene and  $SiO_2$  greatly improves device characteristics, opening up the possibility of ballistic transport [8, 9]. Another promising area of research is the controlled formation of graphene–BN heterostructures, either a stacked or

Address correspondence to hibino.hiroki@lab.ntt.co.jp

hybridized lateral structure, that would make the tuning of the band gap of graphene possible [7, 10, 11].

Similar to graphene, h-BN can be produced by chemical vapor deposition (CVD). For example, CVD-grown monolayer h-BN on single-crystalline metals like Ni(111), Pd(111), and Pt(111) has been reported for more than a decade [12–16]. Further, the growth of h-BN on polycrystalline transition metals have been reported, but so far only yielded few-layer to thick h-BN layers and precise control over the number of layers remains difficult [3, 17–19]. Not until recently has the growth of monolayer h-BN using Cu foil been demonstrated. However, the h-BN film was composed of several domain structures with different orientations most likely due to the polycrystalline nature of the substrate [20].

Here, we report the growth of large-area, monolayer h-BN film on heteroepitaxial Co film supported by a sapphire substrate. The synthesis was carried out by low-pressure chemical vapor deposition (LPCVD) with ammonia–borane (borazane,  $\text{NH}_3\text{--BH}_3$ ) used as the BN precursor. We observed triangular-shaped domains on the order of several micrometers with directions commensurate with the underlying lattice structure of the supporting substrate. Additionally, we found out that once the top layer h-BN has grown, the growth of the second layer becomes very difficult even for prolonged growth times or increased borazane flow rates. This observation is consistent with the earlier finding that the growth rate of the second layer h-BN decreases by more than two orders of magnitude once the first layer has already covered the entire surface [12–14]. In contrast to the growth of graphene on metals with high carbon solubility, the low solubility of nitrogen and boron in Co does not allow thick h-BN to form after CVD. Growth evolution studies also reveal that at the onset of nucleation, the triangular domains formed have two opposite directions, and as the growth progresses, the domains coalesce to cover the entire surface of the substrate.

We introduce for the first time low-energy electron microscopy (LEEM) as a means to determine the number of layers of h-BN films. By measuring the electron reflectivity of the films, accurate determination of the h-BN thickness can be done without a cross-section measurement. The signatures of the reflected

electrons can unambiguously distinguish a monolayer from a bilayer and in principle, up to few-layer h-BN films. The presence of unfilled energy bands in h-BN's electronic band structure calculated using first principles density functional theory (DFT) is responsible for the distinct reflectivity oscillations that are different from graphene's. Thus, this technique can also be used to study 2D graphene–BN heterostructures such as monolayer B–N–C films [11]. As LEEM images can be acquired very quickly, this method will prove to be very useful. This is because most researchers have had to resort to transmission electron microscopy (TEM) to accurately determine the thickness of the film either by suspending the film onto a TEM grid before observation or through a cross-section of the underlying substrate for direct measurement, both of which are time consuming and require careful pre-processing [3, 9, 17–20].

## 2 Results and discussion

### 2.1 Growth and determination of the number of h-BN layers via LEEM

The synthesis of monolayer h-BN was carried out by LPCVD on a Co substrate that was prepared in a manner similar to previous experiments with graphene. Previous reports have indicated that sputtering at elevated temperature creates highly crystalline metal films, whose crystal structure closely follows the structure of the underlying substrate [21–23]. In this experiment, we use c-plane sapphire ( $\alpha\text{-Al}_2\text{O}_3$ ) as our substrate as it produces single crystal Co film [21]. Indeed, the single peak at  $\sim 45^\circ$ , the peak assigned to the (111) diffraction of face-centered cubic (fcc) Co or the (0002) diffraction of hexagonal close-packed (hcp) Co, observed in the X-ray diffraction (XRD) pattern of the sputtered Co film confirms the highly crystalline structure of our Co film (see Fig. S1 in the Electronic Supplementary Material (ESM)). Additionally, we found that exposure to  $\text{H}_2$  immediately before CVD further improves the crystallinity of our substrate as evidenced by the stronger diffraction peak compared to the as-sputtered Co film (Fig. S1(b) in the ESM). Our high CVD growth temperature, suggests that fcc Co(111) is the most likely structure during h-BN growth

as fcc is the most stable structure at temperatures  $> 388\text{ }^{\circ}\text{C}$  [24]. However, further analysis by *ex situ* TEM cross-section and selected area electron diffraction (SAED) suggests that the Co film at room temperature (RT), after CVD is of hcp(0001) structure, as discussed in detail in the ESM (Fig. S2). Sputtering at elevated temperature and the use of c-plane sapphire prove to be important steps in the growth of monolayer h-BN as sputtering Co at room temperature on  $\text{SiO}_2/\text{Si}$  resulted in multilayer h-BN films after CVD [25].

Sample characterization of h-BN is not as direct as in graphene. This is especially true in determining the number of layers because, unlike in graphene, the number of layers in h-BN cannot be precisely determined or estimated by the relative intensities of the Raman peak signals (in graphene's case, a monolayer shows a 2D/G peak intensity ratio greater than two) [26]. Although the Raman peak position and intensity can be used to estimate the number of layers, it does not accurately discriminate a monolayer from bilayer to few-layer h-BN since the peak position is greatly influenced by the substrate, as the number of layers is reduced [27]. Recent studies on CVD-grown h-BN also showed no correlation between the peak position and full width at half maximum (fwhm) with the number of layers [19]. Further, because h-BN is a wide band gap ( $\sim 6\text{ eV}$ ) semiconductor, monolayer h-BN is transparent under an ordinary optical microscope such that the usual optical contrast method that was used for determining graphene's thickness cannot be used for h-BN [20]. Additionally, atomic force microscopy (AFM) studies, especially on transferred CVD-grown h-BN, do not offer fool-proof discrimination between a monolayer from bilayer or even few-layer h-BN as the readings can be affected by the surface roughness of the underlying substrate or the presence of contaminants introduced during transfer.

Figure 1 shows a set of data for our resulting h-BN film. Figure 1(a) is an optical microscope image of our grown h-BN after transferring to a  $\text{SiO}_2(285\text{ nm})/\text{Si}$  substrate. As can be seen, the h-BN film is optically transparent and was only made distinguishable from the substrate by the impurities caused by the polymethylacrylate (PMMA, boundary highlighted by the white dotted line), consistent with an earlier report of monolayer h-BN on  $\text{SiO}_2/\text{Si}$  [20]. To confirm the

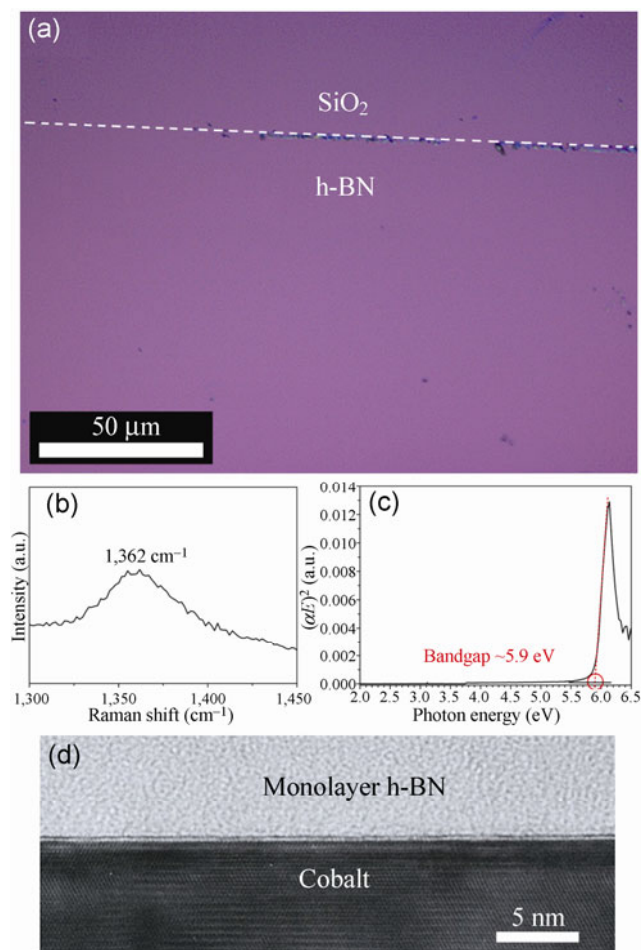


**Figure 1** Characterization of monolayer h-BN. (a) Optical image of h-BN on  $\text{SiO}_2(285\text{ nm})/\text{Si}$ . The h-BN film appears very transparent against the substrate, and the border (white dotted line) is only recognized by the dirt left by the PMMA. (b) Raman spectrum of the film transferred on sapphire excited by a 532-nm laser, showing the signature of h-BN. (c) UV-visible absorption spectra of a monolayer h-BN with a quartz substrate as a reference. The band gap was obtained by taking the x-intercept of the graph (see main text). (d) Cross-section TEM image of the as-grown h-BN film on Co, showing monolayer h-BN.

presence of h-BN, we performed Raman spectroscopy. However, measuring our transferred sample on  $\text{SiO}_2$  proved to be difficult because thin h-BN gives a very weak Raman signal compared to the bulk [27]. A more intense Raman signal appearing at  $1,450\text{ cm}^{-1}$  (arising from the third-order (TO) phonon mode of the silicon substrate) makes the h-BN signal even harder to see. Transferring the h-BN to a transparent sapphire substrate eliminates the unwanted signal and the h-BN shows a distinct Raman peak signal at  $1,362\text{ cm}^{-1}$  as shown in Fig. 1(b). Bulk h-BN is reported to give a

Raman signal at  $\sim 1,365\text{ cm}^{-1}$ , arising from the  $E_{2g}$  phonon mode of the B–N crystal, clearly verifying the presence of h-BN on our sample [28]. The frequency upshift compared to the bulk may be due to local heating induced by our laser source, since we need to use ten times as much power compared to what is normally used for graphene to get a clear Raman signal. Another possibility is that the shift is related to strain, brought about by the substrate or the transfer process. This substrate-induced shift is also common in graphene [29]. Furthermore, UV–visible absorption spectroscopy was performed on the same transferred h-BN sample to validate the presence of h-BN film and determine the band gap of the film. From the equation for a direct band gap semiconductor, the optical band gap can be estimated by plotting the relationship  $(\alpha E)^2 \propto (E - E_g)$ , where  $\alpha$  is the absorbance coefficient,  $E$  is the incident photon energy, and  $E_g$  is the optical band gap, and taking the  $x$ -intercept of the plot (when  $(\alpha E)^2 = 0$ ) (see Fig. S3 in the ESM for details). The resulting graph is shown in Fig. 1(c) and the band gap is found to be  $\sim 5.9\text{ eV}$ . The extrapolated band gap is close to the predicted band gap of  $6\text{ eV}$  for monolayer h-BN, suggesting a thin h-BN film [30]. Finally, the cross-sectional TEM image of our as-grown sample in Fig. 1(d) confirms monolayer h-BN.

Except for the TEM cross-section, the data presented so far confirm the presence of h-BN but do not give much detail about the number of h-BN layers. Accurate, fast, and reliable evaluation of the number of h-BN layers is a very important starting point for clarifying the growth mechanisms as well as for optimizing growth conditions. Further, thickness-dependent h-BN applications such as in electron-tunneling devices require an accurate method for determining the thickness [31]. Previously, LEEM has been used to accurately determine the thickness of graphene films formed on SiC substrate [32]. The method involves measuring the reflectivity of low-energy electrons from thin graphene films and then correlating the number of dips in the reflectivity oscillations to the graphene film thickness. The thickness is determined from the oscillatory behavior in the electron reflectivity spectrum, which is believed to be the result of the resonant electron transmission through the quantized electronic states formed in the thin graphene films.

The number of the quantized states is directly related to the number of graphene layers, and therefore the number of graphene layers can be determined as the number of dips in the reflectivity spectra. In the thick film limit, the quantized states evolve into continuous electronic bands of bulk graphite. Conversely, over the energy windows where graphite has band gaps, incident electrons are reflected at higher probabilities, resulting in broad peaks in the reflectivity spectra.

Similar to the previous work, we used LEEM to measure the thickness of the h-BN films at similar electron energies ranging from  $0$  to  $20\text{ eV}$ . Finding the relationship between reflected electrons and h-BN thickness requires Co surfaces with multilayer h-BN coverages. To achieve this, Co substrates were exposed to BN precursors at increased flow rates for longer times. However, we found that even at higher flow rates and prolonged growth times, only a fraction of the second layer is grown on top of the first layer (see Fig. S4 in the ESM for LEEM images). Figures 2(a) and 2(b) show representative bright-field (BF) LEEM images of the h-BN/Co film grown at  $1$  standard cubic centimeters per minute (sccm) BN precursor flow rate for  $20\text{ min}$ . In the left corner of the image, a small flake can be seen that changes contrast at different electron beam energies. The change in the contrast at different electron beam energies when in the BF mode tells us that the small flake is of different morphology from the background. The small flake is later interpreted as bilayer h-BN. The labels in Fig. 2(b) correspond to the number of layers as identified from the signature of the reflected electrons and, in the case for single layer, from cross-sectional TEM (Fig. 2(c)). Figure 2(d) shows a plot of the reflectivity  $R$ , expressed in intensity, as a function of  $E_e$ , where  $E_e$  is the potential difference between the electron gun and the sample, for the different labeled areas. The area labeled “0” corresponds to the Co substrate, and it showed almost no reflectivity variations for the whole energy spectrum we measured. The areas labeled “1” and “2” in Fig. 2(b) exhibited reflectivity variations reminiscent of the oscillatory behavior of low energy electrons in few-layer graphene [32–35]. Clearly, Fig. 2(d) shows that the spectra from h-BN are different from the spectrum of the bare Co surface. The latter shows no features, but the former clearly show mounds and dips.



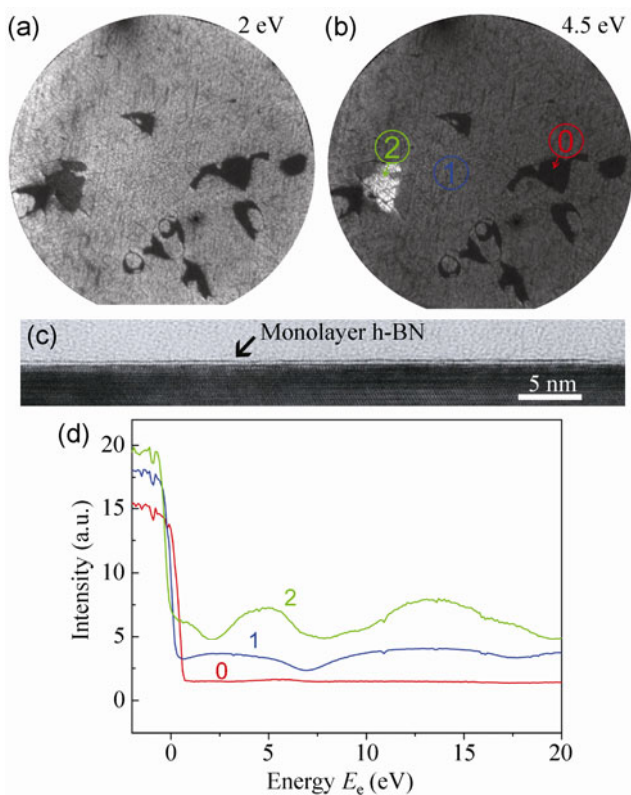


**Figure 2** LEEM observation of monolayer h-BN film. (a), (b) LEEM images of as-grown h-BN film on cobalt at different electron energies. (c) Typical cross-sectional TEM image of the sample showing monolayer h-BN. (d) Reflectivity of the h-BN film at different electron beam energies taken at the corresponding numbered areas of (b). The different numbers correspond to the number of layers; e.g., 1 is monolayer, 2 is bilayer.

Therefore, LEEM can easily distinguish an h-BN sheet from bare Co surface. The nearly flat signal from bare Co, and the reflectivity variations from monolayer h-BN confirmed by cross-sectional TEM, tell us that the reflectivity curves and the actual number of h-BN layers are related.

To interpret our results, we reproduce the positions of the dips in the reflectivity and relate the positions to the energy band structure of h-BN calculated using first principles DFT and crosschecked them using similar reflectivity measurements of graphene grown on SiC(0001) substrate from our previous work [32, 33]. For few-layer graphene (FLG) on SiC(0001), the number of dips in reflectivity corresponds to the number of layers; that is, a single dip corresponds to a monolayer, two dips to a bilayer, and so on. But, between FLG and the SiC substrate, there is an interfacial carbon layer (commonly called a buffer layer), which is structurally

similar to—but electronically different from—graphene. Therefore, the actual number of graphene layers, including the buffer layer, is the number of dips plus one. The dips in reflectivity can be interpreted in the context of quantum mechanics: The energy states are composed of discrete energy levels known as quantum wells (QW) and, as the energy of the incident electrons coincides with one of the QW energy levels, the electrons resonantly transmit through FLG, resulting in dips in the reflectivity. Hence, the oscillatory behavior of FLG can be explained from the band structure of graphite.

Figure 3(a) shows the electronic band structure of graphite in the  $\Gamma$ -A direction, starting at electron energies from the Fermi level,  $E_F$ . Figure 3(b) (top) shows the thickness-dependent reflectivity curves of graphene (as labeled) as a function of electron energy. As can be seen, the low-reflectivity windows ( $0 \text{ eV} < E_e < 7 \text{ eV}$  and  $13 \text{ eV} < E_e < 20 \text{ eV}$ , shaded in green) correspond well to the dispersive unoccupied bands of graphite, while at energies in the range 7–13 eV high reflectivity values are recorded, as a consequence of the absence of energy states. It is important to note, however, that at higher electron energies the electrons have sufficient energy to penetrate the surface and, consequently, the oscillation amplitude is suppressed [34]. This behavior is noticeable at energies between 13 and 20 eV, where the oscillation is almost negligible. Thus, we limit our interpretation to the lower energy regions (0–7 eV).

With h-BN, a similar oscillatory behavior occurs. Figure 3(c) shows the electronic band structure of bulk h-BN along the  $\Gamma$ -A direction as calculated from the first principles method. Accordingly, the dips in reflectivity positions in Fig. 3(b) (bottom) well match the unoccupied energy states (shaded in light blue) in the 0–20 eV energy range. As shown, the presence of the energy band reduces the reflectivity signal, leading to dips in the reflectivity curves. In the region of lowest energy (0–4.5 eV), the presence of the unoccupied states represents well the oscillatory behavior of bilayer h-BN, but no oscillation is observed for monolayer h-BN. Unlike epitaxial monolayer graphene on SiC(0001), where a single dip is clearly seen at  $\sim 3 \text{ eV}$ , monolayer h-BN produces a nearly flat signal. However, considering the buffer layer in SiC-graphene, bilayer h-BN

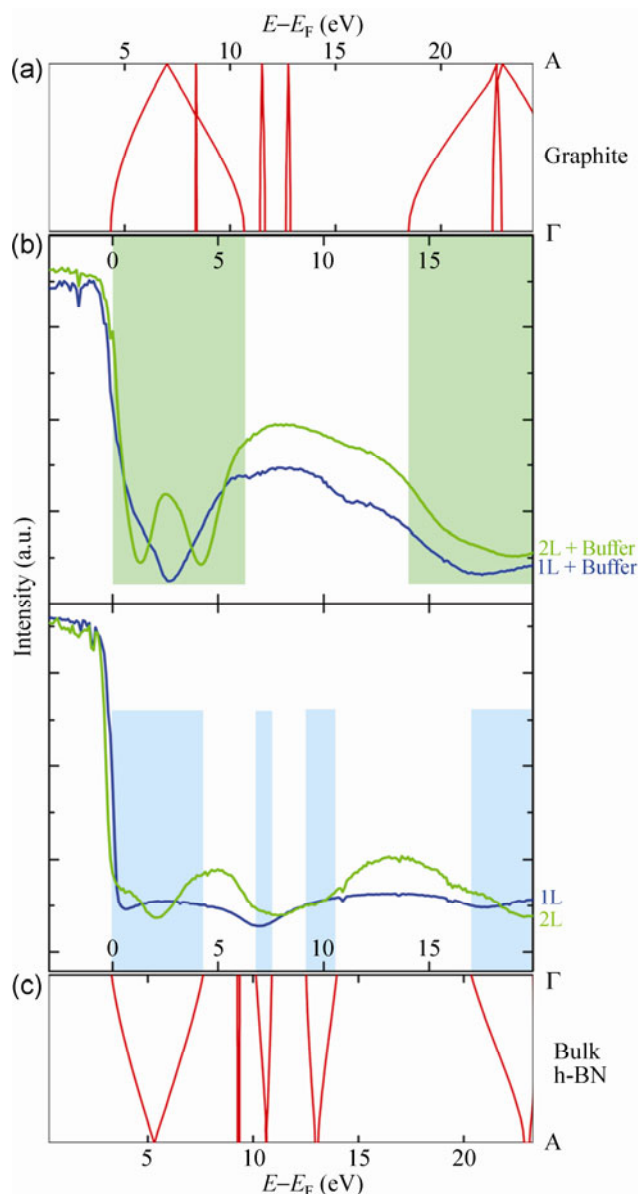


**Figure 3** Reflectivity behavior of graphene and h-BN film. (a) Band structure of graphite in the  $\Gamma$ –A direction, computed using first principles DFT. (b) Reflectivity curves of monolayer and bilayer graphene (top) and h-BN (bottom), showing dips in the lower energy range. The positions of oscillations correspond well to where an unoccupied energy band is located as highlighted by green (for graphene) and blue (for h-BN). The different number of layers produces different oscillations. (c) Calculated band structure of h-BN in the  $\Gamma$ –A direction, computed using first principles DFT.

is expected to behave similarly to monolayer graphene. Indeed, a single dip at  $\sim 2.5$  eV is seen for bilayer h-BN. Further, it is expected that as the number of layers increase, the number of dips also increases with a relationship of  $n = d + 1$ , where  $n$  is the number of

layers and  $d$  is the number of dips within the energy range of 0–4.5 eV. This relationship has been accurately described in graphene on Pt(111), where the film is in direct contact with the metallic substrate [35]. It is expected for our h-BN/Co sample to behave similarly. In this present case, the lack of sufficiently large-area bilayer h-BN, however, prohibits us from performing cross-sectional analysis to verify this relationship.

To explore the possibility of growing additional h-BN films beyond two layers and to support the relationship, similar h-BN growth on Co film using the same growth parameters was performed, but this time the substrate was heated at lower temperature (280 °C) prior to sputtering. Our previous work on h-BN synthesis teaches us that multilayer h-BN can be grown on foils [36]. Since B and N atoms are almost insoluble in Ni or Co at 1,000 °C, a mechanism was proposed that B and N atoms could diffuse through the substrate via grain boundaries, and precipitate on the surface to form the h-BN films. This overall scenario is possible in our experiment, since we expect that sputtering at lower temperature will result to a less crystalline Co film with small grains, and therefore provide pathways for B and N atoms to diffuse through the grain boundaries during CVD, and precipitate to form multilayer h-BN films upon cooling down. Indeed, h-BN films more than two layers thick are grown using this approach. However, we found that the grown h-BN films are not homogenous, with the number of layers varying from two to five within the substrate. Since the primary goal of this experiment is to establish the relationship of LEEM reflectivity dips to the number of h-BN layers, no additional optimization to control the number of layers using this idea was performed. It is interesting to note however, that by just changing the temperature at which the Co film is sputtered, the morphology of the resulting h-BN film can be changed. Although the exact growth mechanism is still not clearly understood, our results should provide a starting point for the investigation towards the production of h-BN with controllable number of layers. Detailed experiments are underway and the results will be published elsewhere. Figure 4(a) shows the bright-field LEEM image of the h-BN films after synthesis on the Co film that was sputtered at lower temperature. The image shows different levels

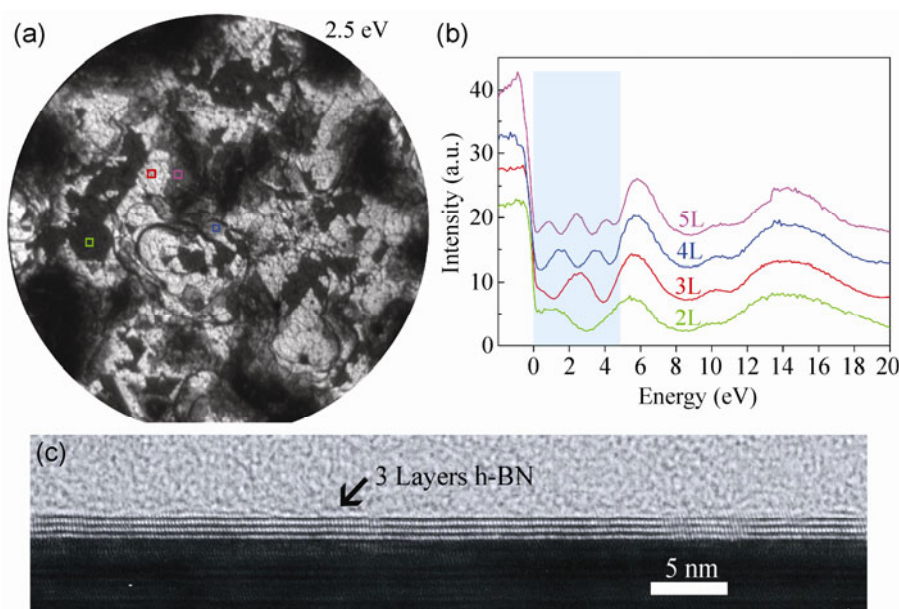


**Figure 4** Low-energy electron reflectivity measurements of few-layer h-BN on Co. (a) LEEM image of the as-grown h-BN film on Co that was sputtered at 280 °C. The resulting film is inhomogeneous as represented by the different levels of brightness of the film. Markers denote areas where the reflectivity curves are taken. (b) Reflectivity curves of the corresponding areas in (a) showing different number of reflectivity dips within the area shaded in light blue (0–4.5 eV). The thickness of the film is determined as the number of dips +1, as labeled. (c) Cross-sectional TEM image of one of the areas in the film showing three layers of h-BN.

of brightness indicating different thickness of the grown film. Reflectivity measurements were taken on the different areas with different levels of contrast (in colored squares), and the corresponding data are presented in Fig. 4(b). In the energy range 0–4.5 eV (shaded in light blue), the different areas gave different number of dips, signifying correlation to the actual number of layers, as discussed above. The actual number of layers is visually verified by taking several cross-sectional TEM images of the sample in Fig. 4(a). The resulting TEM images showed different h-BN layers, with the number of layers about in the same range as what was predicted in our LEEM reflectivity measurements. Figure 4(c) presents a representative TEM image of our sample showing three layers of h-BN, clearly within the predicted range of thickness to support our LEEM measurements.

Another important advantage of the use of LEEM is the possibility of large-scale characterization of B–N–C heterostructures. Both h-BN and graphene domains give different reflectivity curves, with the reflectivity spectra of h-BN having broad dips at 7–13 eV, where those of graphene have broad peaks

(Fig. 3(b)). Graphene and h-BN domains are easily identified in the case where the two different domains coexist on a single substrate due to the different electronic structures of graphene and h-BN.

## 2.2 Incomplete h-BN coverage studies

### 2.2.1 Triangular-shaped h-BN domains

We studied the growth phases of the h-BN film by controlling the growth time and observing the resultant film by LEEM. Such incomplete substrate coverage allows us to investigate the size, shape, and orientation of our h-BN film during the initial stages of the growth. It also allows direct comparison of the h-BN with the underlying Co film. Figure 5(a) shows LEEM images of Co with partial h-BN coverage after exposure to borazane for 4 min. The h-BN film can be easily recognized from the substrate as it appears brighter compared to the Co substrate. Individual triangular domains (bright triangles) with sizes  $> 5 \mu\text{m}$  are seen on the surface of the Co and, in some areas, domain sizes as large as  $20 \mu\text{m}$  are grown (not shown here). The domain sizes are much bigger than in



previous studies performed on other metals [15, 19, 20]. Macroscopically, the shape is very different from the shapes formed in the initial stages of graphene growth (see Ref. [37] for a comprehensive review) and on a similar heteroepitaxial system of h-BN/Ru(0001) [38]. No other initial domain shape was found, except when the triangles coalesce to cover the whole surface. Additionally, two triangles with opposite orientations are observed. Of all the areas we have inspected, we found that these triangles have no preferred direction; i.e., the number of triangles pointing upwards is the same as the number of triangles pointing downwards. More information about the two different domain structures is gained from low-energy electron diffraction (LEED). Shown in Figs. 5(b)–5(d) are the LEED patterns of the three different positions in Fig. 5(a), as labeled accordingly. The Co surface (position 1) shows six first-order diffraction spots, out of which three are dominant, arising from Co(0001) as shown in Fig. 5(b). The relatively weak intensity could be due to the oxidation of Co upon exposure to air [21]. Similarly,

Fig. 5(c) represents the diffraction spots recorded from one of the h-BN triangles (position 2). Six first-order diffraction spots of different intensities are spotted. Further, setting the electron energy in the lower range ( $< 70$  eV) allows us to clearly observe three dominant diffraction spots. In this energy range, the LEED is extremely sensitive to the topmost surface structure; thus, the emergence of the three bright diffraction spots is due to the h-BN. Interestingly, the direction of the diffraction spots matches that of the diffraction spots from the Co substrate. The matched direction and the absence of Moiré diffraction spots on the LEED image suggest a commensurate  $1 \times 1$  structure. Similar to BN/Ni(111), where the small lattice mismatch of  $-0.4\%$  leads to a commensurate  $1 \times 1$  structure, the commensurate structure for BN/Co(0001) ( $+0.4\%$  lattice mismatch) system is expected. On the other hand, the oppositely directed triangle (position 3) showed an almost identical LEED pattern (Fig. 5(d)) but is rotated  $60^\circ$  relative to the first triangle. This implies that the triangular domains must also be rotated  $60^\circ$  relative

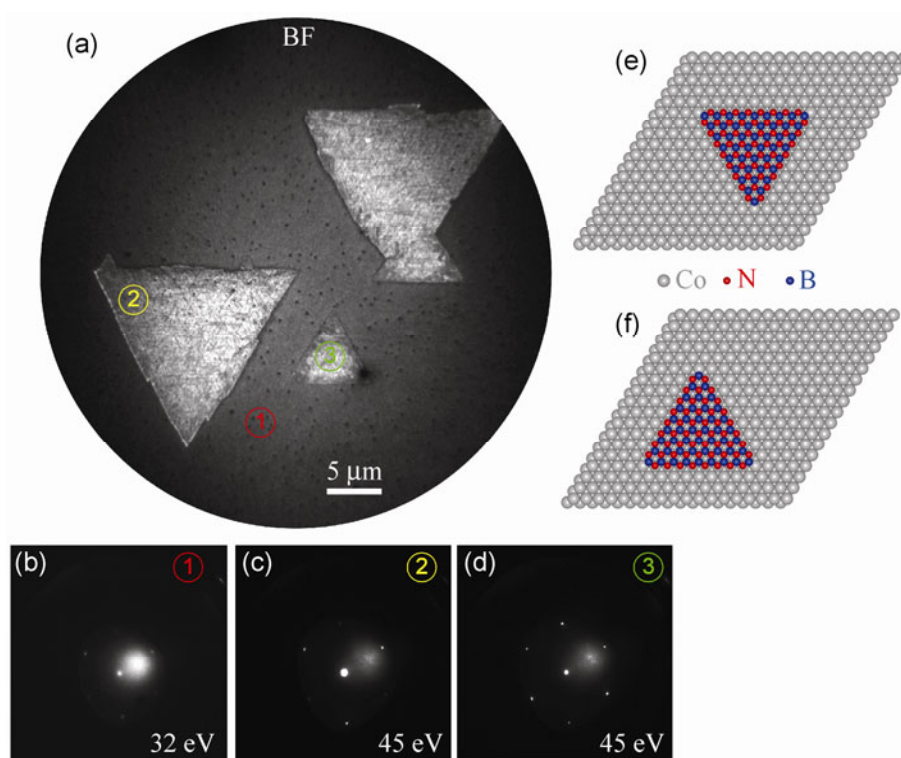


**Figure 5** Incomplete h-BN coverage study on Co film. (a) Bright field (BF) image of h-BN film after exposure to BN precursor for 4 min. The electron beam energy was 5.3 eV. Two triangles having opposite orientations are observed. (b)–(d) LEED patterns of the corresponding labeled areas in (a). (e) and (f) Top views of models representing the two oppositely directed triangles on top of cobalt. The two triangles are N-terminated with the N atom sitting on top of a Co atom (see main text for further discussion).



to each other. Indeed, the two triangles in Fig. 5(a), labeled 2 and 3, are  $60^\circ$  rotated from each other. The orientation of the triangles and the stacking of the BN atoms with respect to the underlying Co atoms can be inferred from the previous experimental and theoretical calculations of similar systems. Similar studies of monolayer h-BN on Ni(111) demonstrated that two h-BN domains of different orientation can coexist on a single-crystal substrate [15, 16]. Furthermore, the arrangement of the adsorbed B atom on the underlying substrate determines the orientation of the triangular domain. These studies suggest that in order for these two triangular domains to form and coexist, the two most stable configurations are as follows: An N atom sitting atop a Ni atom, and a B atom sitting either on fcc (N, B) = (top, fcc) or hcp (N, B) = (top, hcp) hollow sites, respectively. The preference of the N atom to sit directly on top of Ni is due to the strong hybridization of the N lone pair with the Ni atom, as calculated by DFT [39]. Considering the similarity of Ni(111) and Co(0001) in terms of lattice parameters and structure (both have the same close packed surface structure), we argue that our h-BN triangle follows the same configuration.

## 2.2.2 N-terminated h-BN domains and defect lines

Previous theoretical studies also pointed out that the N-terminated zigzag edge is more stable than the B-terminated zigzag edge or the armchair edge in the case when the edge is terminated by H atoms [40]. They also showed that the armchair edge is the most stable configuration for a free standing BN flake. However, armchair edges would result in a domain having a hexagonal shape, therefore a triangular-shaped domain must have zigzag edges. These results suggest that the N-terminated zigzag edge is realized only if dangling bonds of the edge are terminated. In our case, BN flakes are grown on top of the Co surface and the dangling bonds of the BN flake edges are surely terminated by H atoms or Co surface atoms. Consequently, we can deduce that our h-BN triangles are N-terminated. Figures 5(e) and 5(f) represent models for the two triangles that form on the Co substrate.

LEEM provides clear details of the visualization of the domain boundary on a large scale. With the growth of two oppositely directed triangles, the merged domain boundaries can be clearly visualized from the BF LEEM image, as shown in Fig. 6(b). As can be seen,

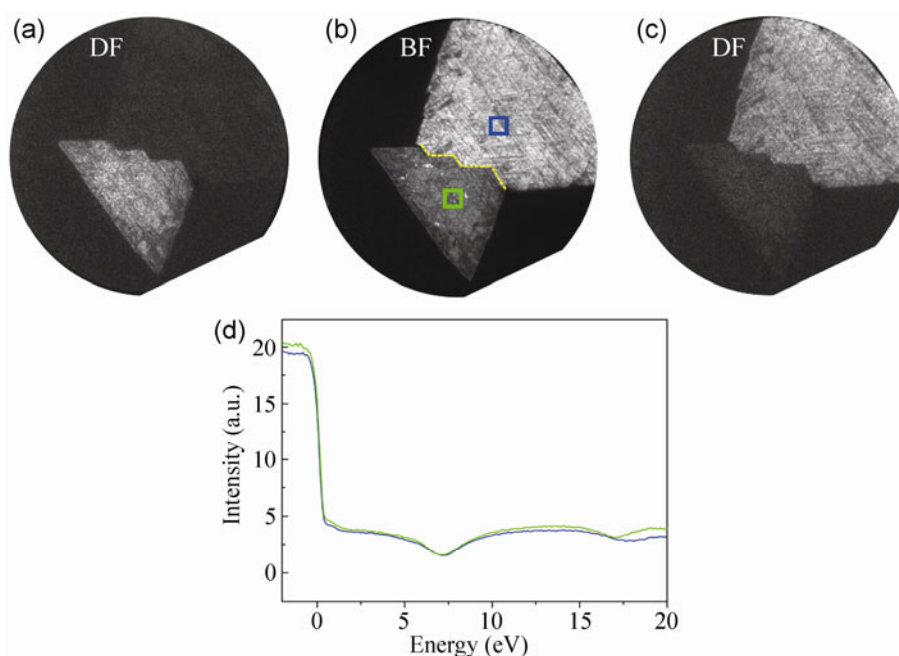


**Figure 6** Merging of two inequivalent h-BN domains. (a)–(c) LEEM images of the merging point of two oppositely oriented triangular domains. The boundary is highlighted by a yellow line in the bright-field (BF) image in (b). (a) and (c) are the dark-field (DF) equivalents of (b). The electron beam energies were 45 eV. (d) Reflectivity curves of the two oppositely directed triangles, showing that the films are monolayer.

two inequivalent domains merge and touch each other, with the boundary highlighted by a yellow line. The dark field (DF) LEEM images using the (1,0) and (0,1) beams, shown in Figs. 6(a) and 6(c), make it possible to distinguish the two domains from each other. The LEEM measurements presented in Fig. 6(d) confirm that these two domains are monolayer h-BN, as identified from the very similar reflectivity spectra to the monolayer h-BN in Fig. 2(d). The factors involved in the origin and control of the initial orientation of these h-BN triangles are not yet well understood, but the different orientations present a remarkable implication—a defect at the domain boundary, as discussed in earlier work [16]. The geometric and chemical structure of the defect at the boundary can only be inferred, as the present LEEM image cannot be used to extract the detailed structure. However, our findings are consistent with the previous findings: The direction of the defect lines supports the N- and B-terminated boundaries and the h-BN growth proceeds in complete hexagonal BN rings up to the proximity of the boundary [16]. As the inequivalent triangular domains grow in size and merge to cover the whole surface, there exists a minimum space for a complete BN hexagon to form, consequently giving rise to line defects at the boundary. It is therefore not possible to have a defect-free h-BN layer from the merging of two differently oriented, N-terminated h-BN domains.

The commensurate  $1 \times 1$  structure also suggests that the orientation of the triangles is directly related to the structure of the substrate. Thus, the initial orientation of the h-BN domains could be influenced by the domain structure of the underlying Co substrate. However, h-BN domains with two opposite directions appear even for single-crystal metal substrate [15]. The initial growth orientation is not fully determined by the underlying substrate but by the interplay of several factors and growth parameters not yet fully understood. Further, previous DFT calculations also taught us that only a slight energy difference determines the registry of the BN hexagons to the underlying substrate and this energy difference is smaller than the thermal energy during h-BN synthesis [39]. Thus, varying the CVD growth temperature may make it possible to control the initial orientation

of the h-BN domains with respect to the underlying Co substrate. However, in similar sub-monolayer coverages experiments at 1,100 °C, h-BN layers did not grow, suggesting a relation between the growth temperature and BN nucleation [15]. In the present case, additional control experiments are needed to achieve single-orientation monolayer h-BN domains. Nonetheless, our results should further promote the understanding of h-BN growth and serve as a step forward towards the tunable growth of h-BN.

### 3 Conclusions

We have shown that the growth of monolayer h-BN films on heteroepitaxial Co metal by LPCVD and characterized them by LEEM. Growth evolution studies reveal that the growth starts with two triangular domains of opposite directions and as the growth progresses, the opposite triangles meet and cover the entire substrate. We found that once the whole substrate is covered with monolayer h-BN, the growth rate is significantly reduced allowing no further growth of additional layers. We also infer from theory and previous experiments that the meeting of the two N-terminated and oppositely directed triangular domains inherently causes a line defect at the boundary.

Additionally, we have introduced for the first time the use of LEEM as a fast and accurate alternative method for determining the number of h-BN layers without a cross-section measurement. Supported by DFT calculations, we show that the unoccupied energy bands of h-BN cause discrete oscillations in the low-energy electron reflectivity spectrum, with the number of dips proportional to the number of layers. LEEM proves to be a powerful tool in investigating the structures of h-BN films, such as their orientation with respect to the underlying substrate, the number of layers, and can even distinguish h-BN from graphene, and should make future investigations of the growth mechanism and optimization easier.

### 4 Experimental section

**CVD synthesis and transfer:** Prior to CVD synthesis, 300 nm thick heteroepitaxial Co films were grown by magnetron sputtering (ULVAC VTR-150M/SRF) on

c-plane sapphire heated at 380 °C at a sputtering rate of 2.5 nm/min (Ar flow rate = 40 sccm, power = 75 W). The h-BN synthesis commenced in a CVD system having two-heating zones: Zone 1 for heating the BN gas precursor (borazane powder) and zone 2 for heating the CVD chamber where the growth run takes place. Borazane powder was used as a precursor because of its non-toxicity and its ability to produce the required BN gas precursors for h-BN synthesis at relatively low temperature, below borazane's melting point of 110 °C [41]. For example, we found out that heating the borazane at 70–80 °C is sufficient to produce the BN precursor gases needed to grow high-quality monolayer h-BN. The growth run started by loading the substrate at the center of the chamber (zone 2) and then pumping the chamber to 2 Torr with H<sub>2</sub>/Ar (20 vol.% H<sub>2</sub>) gas flow. After the growth temperature of 1,000 °C had been reached, the substrate was annealed for 30 min to remove oxide while the same gas flow rates and chamber pressure were maintained. Borazane gas produced after heating zone 1 to the optimum temperature was then introduced to the CVD chamber at a flow rate of 0.5 sccm while the H<sub>2</sub> source was adjusted to 10 sccm and the Ar source was turned off. Growth time was varied depending on the desired h-BN coverage. For example, a 4-minute CVD run only achieved partial coverage while 10 min resulted to full coverage. At the end of the growth run, the borazane source was turned off and the sample was rapidly cooled down to room temperature under H<sub>2</sub>/Ar gases. The film was directly analyzed using LEEM or was transferred to an arbitrary substrate for additional characterization.

To facilitate the transfer, a thin layer of polymethylacrylate (PMMA, Sigma–Aldrich) was spin-coated on top of the h-BN/Co substrate followed by the etching of the Co metal in 0.1 M aq. HNO<sub>3</sub> solution. The typical etching time was 3–5 h. After etching, the PMMA/h-BN that was floating on the etchant was lifted from the surface using a clean glass slide and was transferred into deionized (DI) water to wash away the remaining etchant. The PMMA/h-BN film was washed several times (at least 5x). The PMMA/h-BN was then transferred to the desired substrate (SiO<sub>2</sub>/Si, sapphire, or quartz) by submerging the substrate into

the DI water and picking up the film. The transferred film was allowed to dry in air for 1 h and then heated on top of the hot plate at 90 °C for 30 min. Finally, the PMMA was dissolved in hot acetone (55 °C) for 1 h to complete the transfer process.

**Characterization:** The crystallinity of the Co film was analyzed by XRD using Cu K $\alpha$  radiation (Bruker D2 Phaser). A LEEM instrument (Elmitec LEEM III) was used to obtain bright-field and dark-field images, electron reflectivity measurements, and LEED patterns of the as-grown h-BN films. In detail, the h-BN/Co substrate was loaded into the load-lock chamber and was then transferred to the LEEM chamber with the base pressure of 10<sup>−10</sup> Torr. Characterization then followed after the sample had been annealed up to about 500 °C to remove the adsorbates that were transferred onto it upon exposure to air. TEM images prepared using a focused ion beam (FIB, SII, SMI 3050 SE), were obtained using a Hitachi H-9000 microscope at 300 keV acceleration voltage. Raman data of the transferred film was acquired using a Renishaw Invia spectrometer at 532-nm excitation wavelength. Absorbance (JASCO V-650) was measured at wavelengths 900–200 nm (described in detail in the ESM, Fig. S3).

**First principles calculations:** The first principles calculations were carried out within the local-density functional approximation [42]. The Vanderbilt ultrasoft pseudopotentials were employed for C, B, and N [43]. The exchange-correlation potential was treated within the generalized gradient approximation [44]. The electron wave functions were expanded by using a plane-wave basis set up to 25 Ry. Freedom of spin was not considered. The lattice constant for the h-BN crystal was derived from the previous experimental report [45].

**Electronic Supplementary Material:** X-ray diffraction measurements of the Co film before and after h-BN CVD, high resolution TEM cross-section and SAED pattern of the hcp structure, determination of the band gap from absorption measurements, and a study of h-BN CVD prepared with different flow rates and growth times are available in the online version of this article at <http://dx.doi.org/10.1007/s12274-013-0310-1>.

## References

- [1] Novoselov, K. S.; Jiang, D.; Schedin, F.; Booth, T. J.; Khotkevich, V. V.; Morozov, S. V.; Geim, A. K. Two-dimensional atomic crystals. *Proc. Natl. Acad. Sci. U.S.A.* **2005**, *102*, 10451–10453.
- [2] Neto, A. H. C.; Novoselov, K. New directions in science and technology: Two-dimensional crystals. *Rep. Prog. Phys.* **2011**, *74*, 082501.
- [3] Kim, K. K.; Hsu, A.; Jia, X. T.; Kim, S. M.; Shi, Y. M.; Dresselhaus, M.; Palacios, T.; Kong, J. Synthesis and characterization of hexagonal boron nitride film as a dielectric layer for graphene devices. *ACS Nano* **2012**, *6*, 8583–8590.
- [4] Watanabe, K.; Taniguchi, T.; Kanda, H. Direct-bandgap properties and evidence for ultraviolet lasing of hexagonal boron nitride single crystal. *Nat. Mater.* **2004**, *3*, 404–409.
- [5] Kubota, Y.; Watanabe, K.; Tsuda, O.; Taniguchi, T. Deep ultraviolet light-emitting hexagonal boron nitride synthesized at atmospheric pressure. *Science* **2007**, *317*, 932–934.
- [6] Watanabe, K.; Taniguchi, T.; Niiyama, T.; Miya, K.; Taniguchi, M. Far-ultraviolet plane-emission handheld device based on hexagonal boron nitride. *Nat. Photonics* **2009**, *3*, 591–594.
- [7] Giovannetti, G.; Khomyakov, P. A.; Brocks, G.; Kelly, P. J.; van den Brink, J. Substrate-induced band gap in graphene on hexagonal boron nitride: *Ab initio* density functional calculations. *Phys. Rev. B* **2007**, *76*, 073103.
- [8] Dean, C. R.; Young, A. F.; Meric, I.; Lee, C.; Wang, L.; Sorgenfrei, S.; Watanabe, K.; Taniguchi, T.; Kim, P.; Shepard, K. L.; Hone, J. Boron nitride substrates for high-quality graphene electronics. *Nat. Nanotechnol.* **2010**, *5*, 722–726.
- [9] Lee, K. H.; Shin, H. J.; Lee, J.; Lee, I. Y.; Kim, G. H.; Choi, J. Y.; Kim, S. W. Large-scale synthesis of high-quality hexagonal boron nitride nanosheets for large-area graphene electronics. *Nano Lett.* **2012**, *12*, 714–718.
- [10] Ramasubramanian, A.; Naveh, D.; Towe, E. Tunable band gaps in bilayer graphene–BN heterostructures. *Nano Lett.* **2011**, *11*, 1070–1075.
- [11] Ci, L. J.; Song, L.; Jin, C. H.; Jariwala, D.; Wu, D. X.; Li, Y. J.; Srivastava, A.; Wang, Z. F.; Storr, K.; Balicas, L.; Liu, F.; Ajayan, P. M. Atomic layers of hybridized boron nitride and graphene domains. *Nat. Mater.* **2010**, *9*, 430–435.
- [12] Nagashima, A.; Tejima, N.; Gamou, Y.; Kawai, T.; Oshima, C. Electronic dispersion relations of monolayer hexagonal boron nitride formed on the Ni(111) surface. *Phys. Rev. B* **1995**, *51*, 4606–4613.
- [13] Nagashima, A.; Tejima, N.; Gamou, Y.; Kawai, T.; Oshima, C. Electronic structure of monolayer hexagonal boron nitride physisorbed on metal surfaces. *Phys. Rev. Lett.* **1995**, *75*, 3918–3921.
- [14] Auwärter, W.; Kreutz, T. J.; Greber, T.; Osterwalder, J. XPD and STM investigation of hexagonal boron nitride on Ni(111). *Surf. Sci.* **1999**, *429*, 229–236.
- [15] Auwärter, W.; Suter, H. U.; Sachdev, H.; Greber, T. Synthesis of one monolayer of hexagonal boron nitride on Ni(111) from B-trichloroborazine (CIBNH)<sub>3</sub>. *Chem. Mater.* **2004**, *16*, 343–345.
- [16] Auwärter, W.; Muntwiler, M.; Osterwalder, J.; Greber, T. Defect lines and two-domain structure of hexagonal boron nitride films on Ni(111). *Surf. Sci.* **2003**, *545*, L735–L740.
- [17] Song, L.; Ci, L. J.; Lu, H.; Sorokin, P. B.; Jin, C. H.; Ni, J.; Kvashnin, A. G.; Kvashnin, D. G.; Lou, J.; Yakobson, B. I. et al. Large scale growth and characterization of atomic hexagonal boron nitride layers. *Nano Lett.* **2010**, *10*, 3209–3215.
- [18] Shi, Y. M.; Hamsen, C.; Jia, X. T.; Kim, K. K.; Reina, A.; Hofmann, M.; Hsu, A. L.; Zhang, K.; Li, H. N.; Juang, Z. Y. et al. Synthesis of few-layer hexagonal boron nitride thin film by chemical vapor deposition. *Nano Lett.* **2010**, *10*, 4134–4139.
- [19] Ismach, A.; Chou, H.; Ferrer, D. A.; Wu, Y. P.; McDonnell, S.; Floresca, H. C.; Covacevich, A.; Pope, C.; Piner, R.; Kim, M. J. et al. Toward the controlled synthesis of hexagonal boron nitride films. *ACS Nano* **2012**, *6*, 6378–6385.
- [20] Kim, K. K.; Hsu, A.; Jia, X. T.; Kim, S. M.; Shi, Y. M.; Hofmann, M.; Nezich, D.; Rodriguez-Nieva, J. F.; Dresselhaus, M.; Palacios, T. et al. Synthesis of monolayer hexagonal boron nitride on Cu foil using chemical vapor deposition. *Nano Lett.* **2012**, *12*, 161–166.
- [21] Ago, H.; Ito, Y.; Mizuta, N.; Yoshida, K.; Hu, B. S.; Orofeo, C. M.; Tsuji, M.; Ikeda, K.; Mizuno, S. Epitaxial chemical vapor deposition growth of single-layer graphene over cobalt film crystallized on sapphire. *ACS Nano* **2010**, *4*, 7407–7414.
- [22] Orofeo, C. M.; Ago, H.; Hu, B. S.; Tsuji, M. Synthesis of large area, homogenous, single layer graphene films by annealing amorphous carbon on Co and Ni. *Nano Res.* **2011**, *4*, 531–540.
- [23] Ogawa, Y.; Hu, B. S.; Orofeo, C. M.; Tsuji, M.; Ikeda, K.; Mizuno, S.; Hibino, H.; Ago, H. Domain structure and boundary in single-layer graphene grown on Cu(111) and Cu(100) films. *J. Phys. Chem. Lett.* **2012**, *3*, 219–226.
- [24] Young, D. A. *Phase Diagrams of the Elements*; University of California Press: Berkeley, 1991.
- [25] Suzuki, S.; Hibino, H. Chemical vapor deposition of hexagonal boron nitride. *e-J. Surf. Sci. Nanotech.* **2012**, *10*, 133–138.
- [26] Ferrari, A. C.; Meyer, J. C.; Scardaci, V.; Casiraghi, C.; Lazzeri, M.; Mauri, F.; Piscanec, S.; Jiang, D.; Novoselov, K. S.; Roth, S. et al. Raman spectrum of graphene and graphene layers. *Phys. Rev. Lett.* **2006**, *97*, 187401.



- [27] Gorbachev, R. V.; Riaz, I.; Nair, R. R.; Jalil, R.; Britnell, L.; Belle, B. D.; Hill, E. W.; Novoselov, K. S.; Watanabe, K.; Taniguchi, T. et al. Hunting for monolayer boron nitride: Optical and Raman signatures. *Small* **2011**, *7*, 465–468.
- [28] Reich, S.; Ferrari, A. C.; Arenal, R.; Loiseau, A.; Bello, I.; Robertson, J. Resonant Raman scattering in cubic and hexagonal boron nitride. *Phys. Rev. B* **2005**, *71*, 205201.
- [29] Wang, Y. Y.; Ni, Z. H.; Yu, T.; Shen, Z. X.; Wang, H. M.; Wu, Y. H.; Chen, W.; Wee, A. T. S. Raman studies of monolayer graphene: The substrate effect. *J. Phys. Chem. C* **2008**, *112*, 10637–10640.
- [30] Blase, X.; Rubio, A.; Louie, S. G.; Cohen, M. L. Quasiparticle band structure of bulk hexagonal boron nitride and related systems. *Phys. Rev. B* **1995**, *51*, 6868–6875.
- [31] Britnell, L.; Gorbachev, R. V.; Jalil, R.; Belle, B. D.; Schedin, F.; Katsnelson, M. I.; Eaves, L.; Morozov, S. V.; Mayorov, A. S.; Peres, N. M. R. et al. Electron tunneling through ultrathin boron nitride crystalline barriers. *Nano Lett.* **2012**, *12*, 1707–1710.
- [32] Hibino, H.; Kageshima, H.; Maeda, F.; Nagase, M.; Kobayashi, Y.; Yamaguchi, H. Microscopic thickness determination of thin graphite films formed on SiC from quantized oscillation in reflectivity of low-energy electrons. *Phys. Rev. B* **2008**, *77*, 075413.
- [33] Hibino, H.; Kageshima, H.; Nagase, M. Epitaxial few-layer graphene: Towards single crystal growth. *J. Phys. D: Appl. Phys.* **2010**, *43*, 374005.
- [34] Strocov, V. N.; Blaha, P.; Starnberg, H. I.; Rohlfing, M.; Claessen, R.; Debever, J. M.; Themlin, J. M. Three-dimensional unoccupied band structure of graphite: Very-low-energy electron diffraction and band calculations. *Phys. Rev. B* **2000**, *61*, 4994–5001.
- [35] Sutter, P.; Sadowski, J. T.; Sutter, E. Graphene on Pt(111): Growth and substrate interaction. *Phys. Rev. B* **2009**, *80*, 245411.
- [36] Suzuki, S.; Pallares, R. M.; Hibino, H. Growth of atomically thin hexagonal boron nitride films by diffusion through a metal film and precipitation. *J. Phys. D: Appl. Phys.* **2012**, *45*, 385304.
- [37] Ago, H.; Ogawa, Y.; Tsuji, M.; Mizuno, S.; Hibino, H. Catalytic growth of graphene: Toward large-area single-crystalline graphene. *J. Phys. Chem. Lett.* **2012**, *3*, 2228–2236.
- [38] Sutter, P.; Lahiri, J.; Albrecht, P.; Sutter, E. Chemical vapor deposition and etching of high-quality monolayer hexagonal boron nitride films. *ACS Nano* **2011**, *5*, 7303–7309.
- [39] Grad, G. B.; Blaha, P.; Schwarz, K.; Auwärter, W.; Greber, T. Density functional theory investigation of the geometric and spintronic structure of h-BN/Ni(111) in view of photoemission and STM experiments. *Phys. Rev. B* **2003**, *68*, 085404.
- [40] Liu, Y. Y.; Bhowmick, S.; Yakobson, B. I. BN white graphene with “colorful” edges: The energies and morphology. *Nano Lett.* **2011**, *11*, 3113–3116.
- [41] Frueh, S.; Kellett, R.; Mallery, C.; Molter, T.; Willis, W. S.; King’ondo, C.; Suib, S. L. Pyrolytic decomposition of ammonia borane to boron nitride. *Inorg. Chem.* **2011**, *50*, 783–792.
- [42] Kageshima, H.; Shiraishi, K. Momentum-matrix-element calculation using pseudopotentials. *Phys. Rev. B* **1997**, *56*, 14985–14992.
- [43] Vanderbilt, D. Soft self-consistent pseudopotentials in a generalized eigenvalue formalism. *Phys. Rev. B* **1990**, *41*, 7892–7895.
- [44] Perdew, J. P.; Burke, K.; Ernzerhof, M. Generalized gradient approximation made simple. *Phys. Rev. Lett.* **1996**, *77*, 3865–3868.
- [45] Kurdyumov, A. V.; Solozhenko, V. L.; Zelyavski, W. B. Lattice parameters of boron nitride polymorphous modifications as a function of their crystal-structure perfection. *J. Appl. Cryst.* **1995**, *28*, 540–545.